

## Origin of the Unusual Kinetics of Iron Deposition in Human H-Chain Ferritin

Fadi Bou-Abdallah,<sup>‡</sup> Guanghua Zhao,<sup>‡</sup> Howard R. Mayne,<sup>‡</sup> Paolo Arosio,<sup>§</sup> and N. Dennis Chasteen<sup>\*‡</sup>

Contribution from the Department of Chemistry, University of New Hampshire, Durham, New Hampshire 03824, and Chemistry Section, Faculty of Science, University of Brescia, 25123 Brescia, Italy

Received September 16, 2004; E-mail: ndc@cisunix.unh.edu

**Abstract:** From microorganisms to humans, ferritin plays a central role in the biological management of iron. The ferritins function as iron storage and detoxification proteins by oxidatively depositing iron as a hydrous ferric hydroxide mineral core within their shell-like structures. The mechanism by which the mineral core is formed has been the subject of intense investigation for many years. A diiron ferroxidase site located on the H-chain subunit of vertebrate ferritins catalyzes the oxidation of Fe(II) to Fe(III) by molecular oxygen. A previous stopped-flow kinetics study of a transient  $\mu$ -peroxodiFe(III) intermediate formed at this site revealed very unusual kinetics curves, the shape of which depended markedly on the amount of iron presented to the protein.<sup>17</sup> In the present work, a mathematical model for catalysis is developed that explains the observed kinetics. The model consists of two sequential mechanisms. In the first mechanism, turnover of iron at the ferroxidase site is rapid, resulting in steady-state production of the peroxo intermediate with continual formation of the mineral core until the available Fe(II) in solution is consumed. At this point, the second mechanism comes into play whereby the peroxo intermediate decays and the ferroxidase site is postulated to vacate its complement of iron. The kinetic data reveal for the first time that Fe(II) in excess of that required to saturate the ferroxidase site promotes rapid turnover of Fe(III) at this site and that the ferroxidase site plays a role in catalysis at all levels of iron loading of the protein (48–800 Fe/protein). The data also provide evidence for a second intermediate, a putative hydroperoxodiFe(III) complex, that is a decay product of the peroxo intermediate.

### Introduction

The ferritins are iron detoxification and mineralizing proteins that play a central role in iron homeostasis in animals, plants, and microorganisms.<sup>1–5</sup> Ferritins typically are composed of 24 similar or identical subunits assembled into a shell-like structure inside which Fe(III) is deposited as a stable hydrous ferric oxide mineral core containing several thousand atoms of iron.<sup>1–3</sup> It is now well established that ferritin is not just a passive reservoir for iron, rather the protein has structural attributes that enable it to efficiently harvest iron(II) from its environment. The captured Fe(II) is translocated to the interior of the protein shell via eight hydrophilic channels,<sup>6–11</sup> a process that appears to be

driven by an electrostatic gradient.<sup>12</sup> The H-type subunit of vertebrate ferritins contains a dinuclear iron “ferroxidase site” at which the rapid oxidation of Fe(II) to Fe(III) by dioxygen occurs; subsequent hydrolysis of the Fe(III) and its migration away from the ferroxidase site leads to formation of the Fe(III) mineral core.<sup>13–15</sup>

Iron oxidation/mineralization in human ferritin occurs by at least three reaction pathways.<sup>16,17</sup> After Fe(II) binding at the ferroxidase site,<sup>7,18</sup> the protein-catalyzed oxidation of Fe(II) occurs, H<sub>2</sub>O<sub>2</sub> is the product of O<sub>2</sub> reduction,<sup>19–22</sup> and a mineral

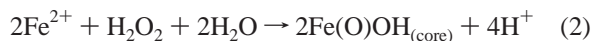
<sup>‡</sup> University of New Hampshire.

<sup>§</sup> University of Brescia.

- (1) Harrison, P. M.; Arosio, P. *Biochim. Biophys. Acta* **1996**, *1275*, 161–203.
- (2) Chasteen, N. D.; Harrison, P. M. *J. Struct. Biol.* **1999**, *126*, 182–194.
- (3) Chasteen, N. D. In *Iron Transport and Storage in Microorganisms, Plants and Animals (Metal Ions in Biological Systems)*; Sigel, A., Sigel, H., Eds.; Marcel Dekker: New York, 1998; Vol. 35, pp 479–514.
- (4) Theil, E. C. In *Handbook of Metalloproteins*; Messerschmidt, A., Huber, R., Poulos, T., Wieghardt, K., Eds.; John Wiley & Sons: Chichester, U.K., 2001; pp 771–781.
- (5) Andrews, S. C. *Adv. Microb. Physiol.* **1998**, *40*, 281–351.
- (6) Bou-Abdallah, F.; Arosio, P.; Levi, S.; Janus-Chandler, C.; Chasteen, N. D. *J. Biol. Inorg. Chem.* **2003**, *8*, 489–497.
- (7) Bou-Abdallah, F.; Arosio, P.; Santambrogio, P.; Yang, X.; Janus-Chandler, C.; Chasteen, N. D. *Biochemistry* **2002**, *41*, 11184–11191.
- (8) Levi, S.; Santambrogio, P.; Corsi, B.; Cozzi, A.; Arosio, P. *Biochem. J.* **1996**, *317*, 467–473.

- (9) Theil, E. C.; Takagi, H.; Small, G. W.; He, L.; Tipton, A. R.; Danger, D. *Inorg. Chim. Acta* **2000**, *297*, 242–251.
- (10) Yang, X.; Arosio, P.; Chasteen, N. D. *Biophys. J.* **2000**, *78*, 2049–2059.
- (11) Barnés, C. M.; Theil, E. C.; Raymond, K. N. *Proc. Natl. Acad. Sci. U.S.A.* **2002**, *99*, 5195–5200.
- (12) Douglas, T.; Ripoll, D. R. *Protein Sci.* **1998**, *7*, 1083–1091.
- (13) Lawson, D. M.; Artymiuk, P. J.; Yewdall, S. J.; Smith, J. M. A.; Livingstone, J. C.; Treffry, A.; Luzzago, A.; Levi, S.; Arosio, P.; Cesareni, G.; Thomas, C. D.; Shaw, W. V.; Harrison, P. M. *Nature* **1991**, *349*, 541–544.
- (14) Liu, X.; Theil, E. C. *Proc. Natl. Acad. Sci. U.S.A.* **2004**, *101*, 8557–8562.
- (15) Harrison, P. M.; Hempstead, P. C.; Artymiuk, P. J.; Andrews, S. C. In *Iron Transport and Storage in Microorganisms, Plants and Animals (Metal Ions in Biological Systems)*; Sigel, A., Sigel, H., Eds.; Marcel Dekker: New York, 1998; Vol. 35, pp 435–478.
- (16) Yang, X.; Chen-Barrett, Y.; Arosio, P.; Chasteen, N. D. *Biochemistry* **1998**, *37*, 9743–9750.
- (17) Zhao, G.; Bou-Abdallah, F.; Arosio, P.; Levi, S.; Janus-Chandler, C.; Chasteen, N. D. *Biochemistry* **2003**, *42*, 3142–3150.
- (18) Treffry, A.; Zhao, Z.; Quail, M. A.; Guest, J. R.; Harrison, P. *Biochemistry* **1997**, *36*, 432–441.

core of Fe(III) is produced, written for simplicity as Fe(O)-OH<sub>(core)</sub> (eq 1). Some of the H<sub>2</sub>O<sub>2</sub> generated in eq 1 reacts with additional Fe(II) in the Fe(II) + H<sub>2</sub>O<sub>2</sub> detoxification reaction (eq 2) to produce H<sub>2</sub>O.<sup>17</sup> Once a mineral core of sufficient size has developed, Fe(II) autoxidation becomes significant and iron oxidation and hydrolysis occur primarily on the growing surface of the mineral through an autocatalytic process where O<sub>2</sub> is reduced completely to H<sub>2</sub>O (eq 3).



Iron oxidation and mineralization in the ferritins from various organisms has been the subject of numerous studies directed at identifying intermediates in the protein-catalyzed pathway (eq 1). Stopped-flow kinetics,<sup>14,18,23–27</sup> resonance Raman spectroscopy,<sup>28</sup> Mössbauer spectroscopy,<sup>25,29</sup> and EXAFS<sup>30</sup> have established that a  $\mu$ -1,2-peroxodiFe(III) intermediate is formed during Fe(II) oxidation by O<sub>2</sub> at the ferroxidase site. This intermediate subsequently decays to one or more  $\mu$ -oxo(hydroxo)-bridged diiron(III) intermediate(s) and small clusters<sup>29–35</sup> whereupon H<sub>2</sub>O<sub>2</sub> is produced in a stoichiometric amount and released into solution.<sup>22,35</sup> The  $\mu$ -oxo(hydroxo)-bridged diFe(III) dimer(s) and clusters ultimately lead to the formation of large polynuclear aggregates and the mineral core itself.

The rapid formation and decay of the  $\mu$ -peroxo diiron(III) intermediate can be conveniently monitored by stopped-flow spectrophotometry due to its blue color ( $\lambda_{\text{max}} \sim 650$  nm).<sup>23–27</sup> In previous stopped-flow experiments employing amounts of iron in excess of 48 Fe/protein, we observed unusually complex behavior in the kinetics of the intermediate that, to our knowledge, had not been previously reported for any ferritin or for any chemical system.<sup>17</sup> In the present paper, we employ multiwavelength stopped-flow spectrophotometry to examine in detail the kinetics of iron uptake by recombinant human H-chain ferritin (a 24mer homopolymer protein that has 24

ferroxidase sites) under conditions of variable iron loading of the protein. A catalytic model for mineralization that accounts for the unusual features of the observed kinetics is presented. The results of the analysis demonstrate that the ferroxidase site is involved in iron oxidation at all levels of iron loading of the protein as the ferroxidase site continually turns over its complement of iron. With increasing iron added to the protein, this protein-catalyzed process occurs to a declining degree as other iron deposition pathways become important. The presence of Fe(II) in excess of that required to saturate the ferroxidase sites of the protein is found to facilitate the turnover of Fe(III) at these catalytic sites. Kinetic and UV–visible spectral data of the 48 Fe/protein sample suggest that the  $\mu$ -peroxodiFe(III) complex is rapidly transformed to another transient species, postulated to be a hydroperoxodiFe(III) complex, that then decays to a more stable  $\mu$ -oxo(hydroxo)diFe(III) complex at the ferroxidase site.

## Materials and Methods

**Protein Preparation.** Recombinant H-chain ferritin (HuHF) was prepared as previously described<sup>36</sup> and rendered iron-free by anaerobic reduction using 55 mM sodium dithionite in 0.1 M Mes (2-(*N*-morpholino)ethanesulfonic acid), pH 6.0, followed by 5 mM dithionite in the same buffer, each for 3 days.<sup>37</sup> The protein was then dialyzed anaerobically under N<sub>2</sub> against 1 mM 2,2'-dipyridyl in 50 mM Mes, pH 6.0, for 2 days to chelate the Fe(II) produced during the reduction,<sup>34</sup> followed by dialysis against 0.1 M Mes, 0.1 M NaCl, pH 6.0, and finally against the 0.1 M Mops (3-(*N*-morpholino)propanesulfonic acid), pH 7.0, the working buffer for the stopped-flow measurements. The concentration of apoHuHF was determined by its absorbance at 280 nm.<sup>22</sup>

**Stopped-Flow Kinetics.** Single wavelength stopped-flow kinetics experiments were performed using a pneumatic drive Hi-Tech SFA-20M stopped-flow accessory with a Varian Cary 50 spectrophotometer as previously described.<sup>17</sup> Multiwavelength stopped-flow measurements were conducted with the Hi-Tech SFA-20M interfaced to a J&M Tidas diode array spectrometer with data acquisition every 2.5 ms in the wavelength range of 190–1024 nm. Equal 140  $\mu$ L volumes of a weakly acidic FeSO<sub>4</sub> (pH 2) and buffered apoferritin solutions under 100% O<sub>2</sub> atmosphere were mixed and shot into the quartz stopped-flow cuvette having a 1 cm path length and a cell volume of 80  $\mu$ L. All concentrations given in the figure captions are final concentrations following mixing of the reagents. The spectrophotometer baseline was determined prior to each kinetic run with a cuvette containing equal volumes of apoferritin in buffer and pH 2 H<sub>2</sub>O. In agreement with the manufacturer's specifications, the dead time of the stopped-flow apparatus itself with the Cary 50 spectrophotometer was determined to be  $6.2 \pm 0.7$  ms using the dichloroindophenol (DICP) and ascorbic acid test reaction.<sup>38</sup> The dead time of the stopped-flow apparatus interfaced to the Tidas diode array spectrometer, including the responses of the hardware and Spectralys 2.00 software plus the 2.5 ms integration time for the first data point, was determined to be  $10.4 \pm 0.4$  ms. For all multiwavelength kinetic runs, this latter dead time was added to the "zero" time, the time corresponding to the first experimental data point collected. A zero–time zero–absorbance point was added to all data sets. Curve fitting was carried out with the derived kinetic equations programmed into Origin, version 7.0, software (OriginLab, Inc.). Best fits were obtained using a combination of Simplex optimization and the Levenberg–Marquardt algorithm. The spectra of the individual components B, B', and C in the postulated reaction pathway A  $\rightarrow$  B  $\rightarrow$

(19) Xu, B.; Chasteen, N. D. *J. Biol. Chem.* **1991**, *266*, 19965–19970.

(20) Waldo, G. S.; Theil, E. C. *Biochemistry* **1993**, *32*, 13262–13269.

(21) Sun, S.; Arosio, P.; Levi, S.; Chasteen, N. D. *Biochemistry* **1993**, *32*, 9362–9369.

(22) Zhao, G.; Bou-Abdallah, F.; Yang, X.; Arosio, P.; Chasteen, N. D. *Biochemistry* **2001**, *40*, 10832–10838.

(23) Treffry, E. C.; Zhao, Z.; Quail, J. R.; Guest, J. R.; Harrison, P. M. *Biochemistry* **1995**, *34*, 15204–15213.

(24) Zhao, Z.; Treffry, A.; Quail, J. R.; Guest, J. R.; Harrison, P. M. *J. Chem. Soc., Dalton Trans.* **1997**, 3977–3978.

(25) Pereira, A. S.; Small, W.; Krebs, C.; Tavares, P.; Edmondson, D. E.; Thiel, E. C.; Huynh, B. H. *Biochemistry* **1998**, *37*, 9871–9876.

(26) Bou-Abdallah, F.; Biasotto, G.; Arosio, P.; Chasteen, N. D. *Biochemistry* **2004**, *43*, 4332–4337.

(27) Fetter, J.; Cohen, J.; Danger, D.; Sanders-Loehr, J.; Theil, E. C. *J. Biol. Inorg. Chem.* **1997**, *2*, 652–661.

(28) Moenne-Loccoz, P.; Krebs, C.; Herlihy, K.; Edmondson, D. E.; Theil, E. C.; Huynh, B. H.; Loehr, T. M. *Biochemistry* **1999**, *38*, 5290–5295.

(29) Bou-Abdallah, F.; Papaefthymiou, G.; Scheswohl, D. S.; Stanga, S.; Arosio, P.; Chasteen, N. D. *Biochem. J.* **2002**, *364*, 57–63.

(30) Hwang, J.; Krebs, C.; Huynh, B. H.; Edmondson, D. E.; Theil, E. C.; Penner-Hahn, J. E. *Science* **2000**, *287*, 122–125.

(31) Bauminger, E. R.; Harrison, P. M.; Hechel, D.; Hodson, N. W.; Nowik, I.; Treffry, A. *Biochem. J.* **1993**, *296*, 709–719.

(32) Treffry, A.; Bauminger, E. R.; Hechel, D.; Hodson, N. W.; Nowik, I.; Yewdall, S. J.; Harrison, P. M. *Biochem. J.* **1993**, *296*, 721–728.

(33) Bauminger, E. R.; Harrison, P. M.; Hechel, D.; Nowik, I.; Treffry, A. *Biochim. Biophys. Acta* **1991**, *1118*, 48–58.

(34) Bauminger, E. R.; Harrison, P. M.; Nowik, I.; Treffry, A. *Biochemistry* **1989**, *28*, 5486–5493.

(35) Jameson, G. N. L.; Jin, W.; Krebs, C.; Perreira, A. S.; Tavares, P.; Liu, X.; Theil, E. C.; Huynh, B. H. *Biochemistry* **2002**, *41*, 13435–13443.

(36) Santambrogio, P.; Cozzi, A.; Levi, S.; Rovida, E.; Magni, F.; Albertine, A.; Arosio, P. *Protein Expression Purif.* **2000**, *19*, 212–218.

(37) Treffry, A.; Hirtzmann, J.; Yewdall, S. J.; Harrison, P. M. *FEBS Lett.* **1992**, *302*, 108–112.

(38) Tonomura, B.; Nakatani, H.; Ohnishi, M.; Yamaguchi-Ito, J.; Hiromi, K. *Anal. Biochem.* **1978**, *84*, 370–383.

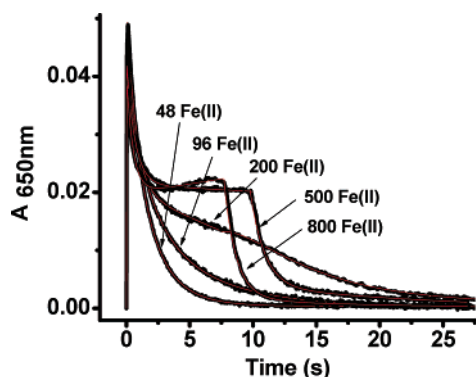


**Figure 1.** Family of stopped-flow kinetic curves at 650 nm for different iron loadings of human H-chain apoferritin. Simulated curves (red) are also shown and fall within the noise of each kinetic trace. The kinetic parameters derived from curve fitting of each curve are given in Table 1. Conditions: 3  $\mu\text{M}$  ferritin saturated with 100%  $\text{O}_2$ , 144–2400  $\mu\text{M}$   $\text{FeSO}_4$  (pH 2.0) saturated with 100%  $\text{O}_2$ , 100 mM Mops, pH = 7.0, 25  $^\circ\text{C}$ . The experimental curves are reproduced from ref 17 with permission.

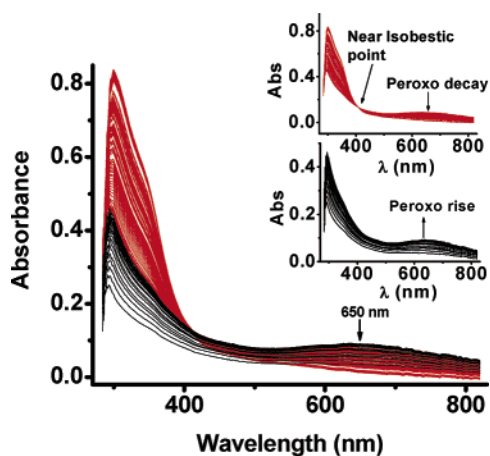


**Figure 2.** Family of stopped-flow UV-visible spectra for a 48 Fe/protein sample. Lower inset: Subfamily of spectra showing the expanded visible region for the formation of the intermediates in the first 50 ms of the reaction. The rise in the peroxo complex is indicated in black and its decay in red. Upper inset: Subfamily of spectra showing the expanded visible region for the decay of the intermediate(s) in the time interval of 50 ms to 14 s. Spectra were gathered every 2.5 ms for the first 0.16 s of the reaction and every 17.5 ms thereafter. Conditions: 5.0  $\mu\text{M}$  ferritin saturated with 100%  $\text{O}_2$ , 240  $\mu\text{M}$   $\text{FeSO}_4$  (pH 2.0) in air, 100 mM Mops, pH = 7.0, 25  $^\circ\text{C}$ . The protein used is from a preparation different from that in Figure 1.

$B' \rightarrow C$  were obtained by solving the set of three simultaneous linear equations of the form  $Y(\lambda, t) = \epsilon_B(\lambda)[B(t)] + \epsilon_{B'}(\lambda)[B'(t)] + \epsilon_C(\lambda)[C(t)]$ , where  $Y(\lambda, t)$  is absorbance and the  $\epsilon$  values are the unknown individual molar absorptivities. The three equations chosen corresponded to the times where each of the three species achieved its maximum concentration, namely,  $t = 50$  ms, 800 ms, and 20 s for species  $B$ ,  $B'$ , and  $C$ , respectively.

## Results

Stopped-flow experiments were carried out in which Fe(II) was shot against the apoprotein using Fe/protein ratios of 48, 96, 200, 500, and 800. Figure 1 shows the previously reported<sup>17</sup> family of stopped-flow kinetic traces at 650 nm for the formation and decay of the  $\mu$ -peroxodiFe(III) intermediate for different levels of Fe(II) added to recombinant human H-chain ferritin (HuHF) under an atmosphere of 100%  $\text{O}_2$ . For ease of comparison, the different kinetic curves in Figure 1 have been shifted on the ordinate axis such that the final absorbance of each is zero. The 48 Fe(II)/protein sample, where just enough

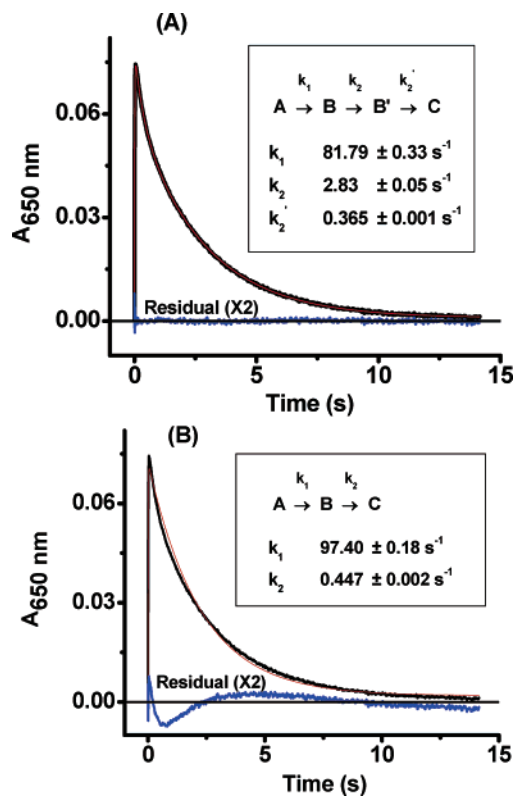


**Figure 3.** Absorbance–time curve at 650 nm from the data in Figure 2. (A) Experimental (black), simulated (red), and residual (blue) curves for the assumed reaction sequence  $A \rightarrow B \rightarrow B' \rightarrow C$ . The rate constants from the simulation are  $k_1 = 81.8 \pm 0.3$ ,  $k_2 = 2.83 \pm 0.05$ , and  $k_2' = 0.365 \pm 0.001 \text{ s}^{-1}$  with  $\chi^2 = 0.705 \times 10^{-6}$ . This sample is from a protein preparation different from that in Table 1, and therefore the rate constants differ slightly. (B) Experimental (black), simulated (red), and residual (blue) curves for the assumed reaction sequence  $A \rightarrow B \rightarrow C$ . The rate constants for the simulation are  $k_1 = 97.4 \pm 0.2$  and  $k_2 = 0.447 \pm 0.002 \text{ s}^{-1}$  with  $\chi^2 = 2.39 \times 10^{-6}$ . A significantly poorer fit is obtained with this model. The horizontal line at  $A_{650} = 0.0$  represents a hypothetical zero residual upon which the calculated residual (multiplied by 2 for clarity) is superimposed.

Fe(II) has been added to completely saturate the 24 ferroxidase sites with iron, exhibits the simplest kinetic behavior. Increasingly complex kinetic profiles are observed as the amount of Fe(II) added to the protein is increased; the pronounced shoulder seen for the 200 Fe sample develops into a plateau with the 500 and 800 Fe samples.

**Kinetics of a 48 Fe/Protein Sample.** We first consider in some detail the kinetics of a 48 Fe/protein sample. Figure 2 illustrates the family of UV-visible reaction spectra obtained when 48 Fe(II) are shot against the apoprotein in a multiwavelength stopped-flow experiment. Absorbance maxima occur at  $\sim 305$  and  $\sim 650$  nm. The lower inset shows the series of spectra for the first 50 ms of the reaction where the concentration of the peroxo intermediate ( $\lambda_{\text{max}} \sim 650$  nm) increases and reaches a maximum; the upper inset illustrates the series of spectra for the decay of the intermediate in the time interval of 50 ms to 14 s. A pure isobestic point is not obtained in the top inset of Figure 2, indicating the presence of more than one decay product of the peroxo intermediate. After we tried several kinetic models, the 650 nm data for the 48 Fe(II)/protein sample were best fitted (Figure 3A) according to a sequential reaction of the type



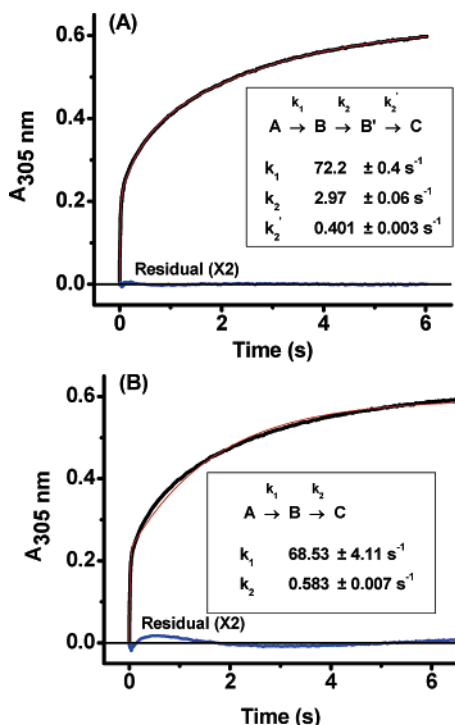


**Figure 4.** Absorbance–time curve at 305 nm from the data in Figure 2. Experimental (black), simulated (red), and residual (blue) curves are shown. The rate constants from the simulation are  $k_1 = 72.2 \pm 0.4$ ,  $k_2 = 2.97 \pm 0.06$ , and  $k_2' = 0.401 \pm 0.003 \text{ s}^{-1}$  of eq 4 with  $\chi^2 = 2.3 \times 10^{-6}$ . (B) Experimental (black), simulated (red), and residual (blue) curves for the assumed reaction sequence  $A \rightarrow B \rightarrow C$ . The rate constants for the simulation are  $k_1 = 68.53 \pm 4.11$  and  $k_2 = 0.583 \pm 0.007 \text{ s}^{-1}$  with  $\chi^2 = 5.0 \times 10^{-5}$ . A significantly poorer fit is obtained with this model. The horizontal line at  $A_{650} = 0.0$  represents a hypothetical zero residual upon which the calculated residual (multiplied by 2 for clarity) is superimposed.

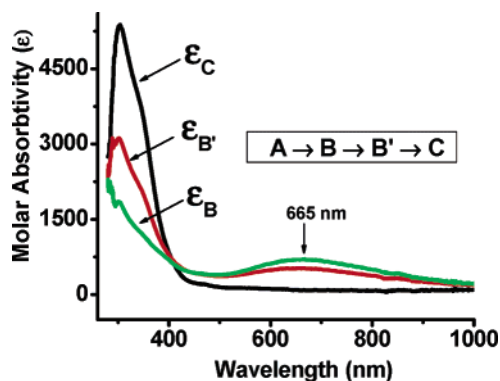


**Figure 5.** Spectra of individual components B (green), B' (red), and C (black) from deconvolution of the reaction spectra in Figure 2.

Very similar curve fitting results for the model in eq 4 were obtained with protein samples from five different protein preparations/purifications or when 24 or 48 Fe(II) were shot against the protein, indicating that the observed kinetics are not sample dependent and that at least two intermediates, B and B', can be consistently resolved in the rate data. As shown in Figure 3B, a significantly poorer fit to the data and a corresponding large residual were obtained with the simpler scheme,  $A \rightarrow B \rightarrow C$ . Similarly, the reaction scheme  $A \rightarrow B$  plus  $B \rightarrow C$  and  $B \rightarrow C'$  or  $A \rightarrow B \rightarrow C$  plus  $A \rightarrow B' \rightarrow C'$  was found to either give poorer fits to the kinetic data or resulted in physically meaningless values of the rate constants with 10- to 1000-fold errors and negative molar absorptivities for some species with similarly

large errors (not shown), indicating strong correlation between the fitting parameters and inappropriateness of these models. Nevertheless, the fitting results reported here do not preclude the possibility that the data, while appearing to conform to eq 4 very well, are in fact due to another kinetic process not yet considered.

In eq 4, A represents a “ferrous–dioxygen–protein” complex at the ferroxidase site that reacts quickly by a first-order process with a rate constant ( $k_1$ ) to form the  $\mu$ -peroxodiFe(III) intermediate B. Intermediate B subsequently decays with rate constant  $k_2$  to form a related colored complex (B') that is then transformed to the final species C. The identities of the B' and C species are considered below. For simplicity of notation, reactants and products, such as  $\text{H}^+$ ,  $\text{H}_2\text{O}$ , and  $\text{H}_2\text{O}_2$ , that enter the chemistry of eq 1 have been omitted from the reaction scheme above (eq 4).

The absorbance–time curves at 650 and 305 nm are shown in Figures 3 and 4, respectively. The absorbance,  $Y(\lambda, t)$ , as a function of time was fitted to the equation  $Y(\lambda, t) = \epsilon_B(\lambda)[B(t)] + \epsilon_{B'}(\lambda)[B'(t)] + \epsilon_C(\lambda)[C(t)]$ , where the  $\epsilon$  values are molar absorptivities of the species at the specified wavelength. The concentrations of the various species are given by the following integrated rate law equations for a four-step consecutive first-order reaction:<sup>39</sup>

$$A(t) = A_0 e^{-k_1 t} \quad (5)$$

$$B(t) = \frac{k_1 A_0}{k_2 - k_1} (e^{-k_1 t} - e^{-k_2 t}) \quad (6)$$

$$B'(t) = A_0 \left[ \frac{k_1 k_2}{(k_2' - k_1)(k_2 - k_1)} e^{-k_1 t} - \frac{k_1 k_2}{(k_2' - k_2)(k_2 - k_1)} e^{-k_2 t} + \frac{k_1 k_2}{(k_2' - k_2)(k_2' - k_1)} e^{-k_2' t} \right] \quad (7)$$

$$C(t) = A_0 \left[ 1 - \frac{k_2 k_2'}{(k_2 - k_1)(k_2' - k_1)} e^{-k_1 t} - \frac{k_1 k_2'}{(k_1 - k_2)(k_2' - k_2)} e^{-k_2 t} - \frac{k_1 k_2}{(k_1 - k_2')(k_2 - k_2')} e^{-k_2' t} \right] \quad (8)$$

The model fits the observed kinetics very well, and good correspondence is obtained between the rate constants  $k_1$ ,  $k_2$ , and  $k_2'$  from the data for the two wavelengths (Figures 3A and 4A).

**Component Spectra for the 48 Fe/Protein Sample.** The spectra of the individual species, that is,  $\epsilon_B(\lambda)$ ,  $\epsilon_{B'}(\lambda)$ , and  $\epsilon_C(\lambda)$  versus  $\lambda$ , were obtained by deconvolution of the reaction spectra of Figure 2. The results are shown in Figure 5. The diFe(III) peroxo complex B shows the characteristic absorbance at 665 nm ( $\epsilon_B(665 \text{ nm}) = 840 \pm 170 \text{ cm}^{-1} \text{ M}^{-1}/\text{Fe(III) dimer}$ ,  $N = 5$ ) with a second band at 300 nm ( $\epsilon_B(300 \text{ nm}) = 1855 \pm 370 \text{ cm}^{-1} \text{ M}^{-1}/\text{dimer}$ ). Species B' also absorbs in the visible region ( $\lambda_{\text{max}} = 655 \text{ nm}$ ,  $\epsilon_{B'}(655 \text{ nm}) = 570 \pm 125 \text{ cm}^{-1} \text{ M}^{-1}/\text{dimer}$ ) with a second band in the ultraviolet ( $\lambda_{\text{max}} = 302 \text{ nm}$ ,  $\epsilon_{B'}(302 \text{ nm}) = 3120 \pm 620 \text{ cm}^{-1} \text{ M}^{-1}/\text{dimer}$ ). Its spectral properties suggest a peroxo species that we postulate as a

(39) Rodiquin, N. M.; Rodiquina, E. N. *Consecutive Chemical Reactions: Mathematical Analysis and Development*; D. van Nostrand Co. Inc.: Princeton, NJ, 1964; pp 7–9.

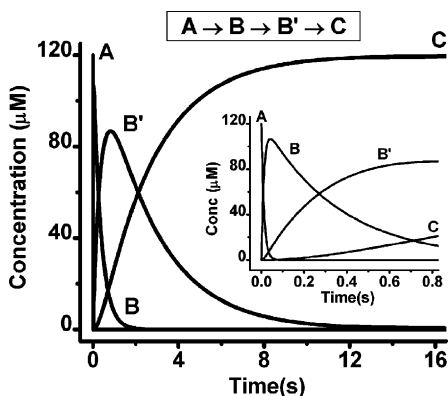
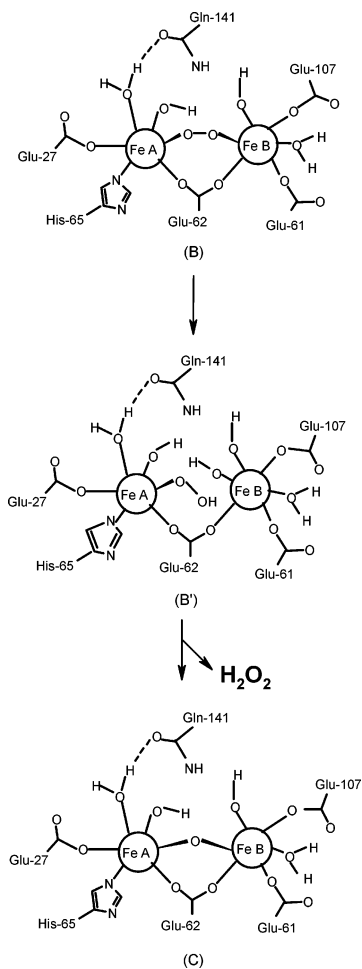


**Figure 6.** Simulation of the concentrations of A, B, B', and C species as a function of time using the rate constants in Figure 3A. The inset shows the early portion of the simulation.

**Scheme 1.** Postulated Ferroxidase Site Species Transformations



hydroperoxo complex formed in the pathway to release  $\text{H}_2\text{O}_2$  from the diFe(III) center into the bulk solution (Scheme 1). The visible band maxima and molar absorptivities given above for species B and B' fall within the range of values reported for high-spin Fe(III) peroxo compounds.<sup>25,40,41</sup> The spectrum of species C has a maximal absorbance at 305 nm ( $\epsilon_{\text{C}}(305 \text{ nm}) = 5380 \pm 1700 \text{ cm}^{-1} \text{ M}^{-1}/\text{dimer}$ ) and is similar to that of the previously reported  $\mu$ -1,2-oxo(hydroxo)diFe(III) complex.<sup>16,29</sup>

(40) Tshuva, E. Y.; Lippard, S. J. *J. Chem. Rev.* **2004**, *104*, 987–1012.

(41) Costas, M.; Mehn, M. P.; Jensen, M. P.; Que, L., Jr. *J. Chem. Rev.* **2004**, *104*, 939–986.

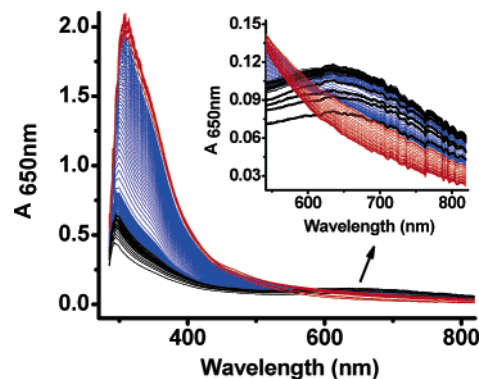


**Figure 7.** Family of stopped-flow UV–visible spectra for a 500 Fe/protein sample. Inset: Family of spectra showing the expanded visible region for the formation and decay of the peroxo intermediate. Spectra were gathered every 2.5 ms for the first 0.160 s of the reaction and every 62.5 ms thereafter. The rise in peroxo intermediate is indicated in black, its initial decay and plateau in blue, and its final decay in red. Conditions: 5.35  $\mu\text{M}$  ferritin saturated with 100%  $\text{O}_2$ , 100 mM Mops, pH = 7.0, 25  $^\circ\text{C}$ . The protein used is from a preparation different from that in Figure 1 but the same as that in Figure 2.

**Species–Time Profiles for the 48 Fe/Protein Sample.** Figure 6 shows the concentration–time profiles of the various species computed from the integrated rate equations (eqs 5–8). The A species rapidly decays (half-life  $t_1 = 8.5$  ms) to form the peroxo complex B. The peroxo complex reaches a maximal concentration at approximately 50 ms (not 160 ms as previously reported<sup>17,23</sup>) and then decays with a half-life time of  $t_2 = 0.25$  s to the putative hydroperoxo complex B'. The B' species achieves its maximal concentration in approximately 0.83 s and then decays with a half-life  $t_2' = 1.9$  s to form the  $\mu$ -oxo-(hydroxo)diFe(III) complex C. The entire Fe(II) oxidation reaction is complete within  $\sim 10$  s.

**Kinetics of >48 Fe/Protein Samples.** Figure 7 illustrates the family of reaction spectra obtained for a sample in which 500 Fe are shot against apoHuHF. The inset of Figure 7 shows a complex pattern of spectral curves associated with the kinetics of the peroxo intermediate B. The 650 nm kinetic trace for the intermediate is illustrated in Figure 8. After a rapid initial rise and partial decay, an absorbance plateau is formed in the time period of 0.9–3.2 s. The time over which the plateau occurs depends on the protein preparation used. For example, with the 500 Fe(II)/protein sample of Figure 1, the plateau extends to a time of 9.9 s. Nevertheless, as illustrated below, the rate constants obtained from kinetic analysis of different protein preparations are quite similar, the samples differing only in the percentage of iron that is processed by the ferroxidase site reaction in each case.

The presence of a plateau in absorbance indicates that the intermediate B forms and decays at the same rate and thus achieves steady-state in concentration. The continual formation of the peroxo intermediate demonstrates that ferritin maintains catalytic activity well beyond oxidation of the first 48 Fe(II) and therefore behaves as a true enzyme as previously postulated.<sup>21</sup> Beyond 3.2 s, the intermediate begins to disappear and is completely gone within 15 s from the start of the reaction (Figures 1 and 8). The nonzero absorbance seen at the end of the kinetic in Figure 8 is due to a strong UV absorbance (maximum near 300 nm) that tails into the visible region from polynuclear iron.

**Mechanism I of the >48 Fe/Protein Sample.** After trying several approaches to simulating the data, we adopted the

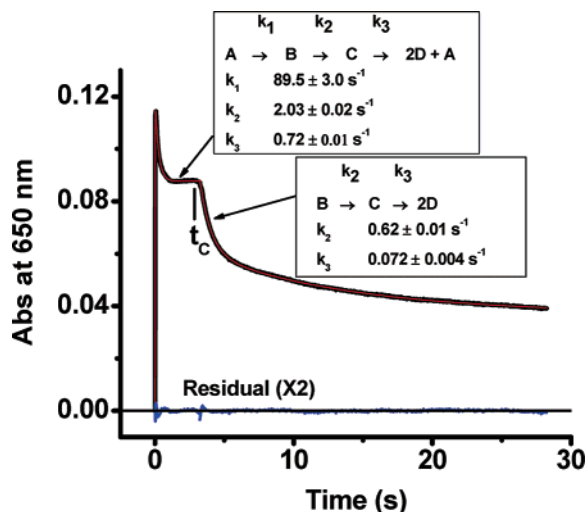
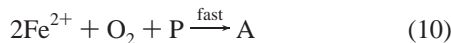


**Figure 8.** Absorbance–time curve at 650 nm from the data in Figure 7. Experimental (black), simulated (red), and residual (blue) curves are shown. The rate constants from the simulation are  $k_1 = 89.5 \pm 3.0$ ,  $k_2 = 2.03 \pm 0.02$ , and  $k_3 = 0.72 \pm 0.01 \text{ s}^{-1}$  for Mechanism I and  $k_2 = 0.62 \pm 0.01$  and  $k_3 = 0.072 \pm 0.004 \text{ s}^{-1}$  for Mechanism II with  $t_c = 3.2 \text{ s}$ . The protein preparation is different from that in Figure 1 and Table 1, and therefore the rate constants differ somewhat from those in Table 1. The flat horizontal line at  $A_{650} = 0.0$  represents a hypothetical zero residual upon which the calculated residual (multiplied by 2 for clarity) is superimposed.

following model for the kinetics in the time interval of 0–3.2 s, that is, from the start of the reaction to the end of the plateau in Figure 8.



The product D in eq 9 represents the total iron accumulated in the mineral core expressed on a per Fe(III) basis; P represents the vacated protein ferroxidase site. P rapidly recycles via eq 10 to regenerate species A, the reactive Fe(II)–O<sub>2</sub>–protein complex that leads to the  $\mu$ -peroxodiFe(III) complex B of eq 9. Intermediate B then decays to the  $\mu$ -oxodiFe(III) complex C. Translocation of the Fe(III) from the ferroxidase site to the core D regenerates the vacated ferroxidase site P. The stoichiometric coefficient of 2 of eq 9 reflects the fact that C is a dimer that decays to D expressed on monomeric Fe(III) basis. The postulated “hydroperoxy species” B’ observed in the 48 Fe sample (i.e., eq 4) was not kinetically resolved in the 500 Fe/protein data, where the protein is flooded with iron and therefore not included as part of the model. It is, perhaps, transiently formed in low concentration under the conditions of high iron loading of the protein or is difficult to resolve from the multiple iron deposition reactions that are occurring simultaneously at such high levels of iron (eqs 1–3), as reflected in the lack of an isobestic point in Figure 7. In addition, when large amounts of Fe(II) are added (96–800 Fe/protein), the shoulder that develops occurs in the time domain where the species B’ also appears, making it difficult to distinguish its presence.

The vacated ferroxidase site P produced in eq 9 is rapidly converted to A through eq 10, a process requiring <50 ms.<sup>18</sup> Thus, to a good approximation, the kinetics conform to the following net equation:



Equation 11 describes a cyclic process that continually produces the mineral core D while regenerating the reactive species A. This process is maintained as long as there is sufficient Fe(II) and O<sub>2</sub> available for production of species A from species P through eq 10. The appropriate differential equations for this mechanism (Mechanism I) are given by the following expressions:

$$d[A]/dt = -k_1[A] + k_3[C] \quad (12)$$

$$d[B]/dt = k_1[A] - k_2[B] \quad (13)$$

$$d[C]/dt = k_2[B] - k_3[C] \quad (14)$$

$$d[D]/dt = 2k_3[C] \quad (15)$$

By applying the method of Laplace transforms,<sup>42</sup> we arrive at the following integrated rate laws for the concentrations of each of the four species as a function of time.

$$A(t) = A_0 \times \left\{ \left[ \frac{a^2 + (\gamma - a)(k_2 + k_3)}{a(a - b)} \right] e^{-at} - \left[ \frac{b^2 + (\gamma - b)(k_2 + k_3)}{b(a - b)} \right] e^{-bt} + \left[ \frac{\gamma(k_2 + k_3)}{ab} \right] \right\} \quad (16)$$

$$B(t) = A_0 \times \left[ \frac{k_1(k_3 - a)}{a(a - b)} e^{-at} - \frac{k_1(k_3 - b)}{b(a - b)} e^{-bt} + \frac{k_1 k_3}{ab} \right] \quad (17)$$

$$C(t) = A_0 \times \{1 - P e^{-at} + Q e^{-bt} - R\} \quad (18)$$

$$D(t) = \int_0^t 2k_3 C(t) dt = 2k_3 A_0 \left[ (1 - R)t + \frac{P}{a} (e^{-at} - 1) + \frac{Q}{b} (1 - e^{-bt}) \right] \quad (19)$$

where

$$P = \frac{a^2 + (\gamma - a)(k_2 + k_3) + k_1(k_3 - a)}{a(a - b)} \quad (20)$$

$$Q = \frac{b^2 + (\gamma - b)(k_2 + k_3) + k_1(k_3 - b)}{b(a - b)} \quad (21)$$

$$R = \frac{\gamma(k_2 + k_3) + k_1 k_3}{ab} \quad (22)$$

Here,  $a = 1/2(\alpha - \sqrt{\alpha^2 - 4\beta})$ ,  $b = 1/2(\alpha + \sqrt{\alpha^2 - 4\beta})$ ,  $\alpha = k_1 + k_2 + k_3$ ,  $\beta = k_1 k_2 + k_2 k_3 + k_1 k_3$ , and  $\gamma = k_2 k_3 / (k_2 + k_3)$ .  $A_0$  is the concentration of ferroxidase sites and is 24 times the protein concentration.

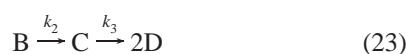
**Mechanism II of the >48 Fe/Protein Sample.** We attribute the fall off in absorbance at the end of the plateau for the 500 Fe sample to decay of the colored intermediate B due to consumption of all the available Fe(II) (Figure 8). (Parallel kinetic measurements under the same conditions in an oximetry cell showed that some O<sub>2</sub> remains in solution at the end of the re-

(42) Steinfeld, J. I.; Francisco, J. S.; Hase, W. L. *Chemical Kinetics and Dynamics*; Prentice Hall: Englewood Cliffs, NJ, 1989; pp 48–53.

**Table 1.** Kinetic Parameters for the 650 nm Data of Figure 1

| Fe/shell | Mechanism I (>48 Fe)<br>$A \xrightarrow{k_1} B \xrightarrow{k_2} B' \xrightarrow{k_2'} C$<br>$A \xrightarrow{k_1} B \xrightarrow{k_2} C \xrightarrow{k_3} 2D+A$ |                          |                           |                          | Mechanism II (>48 Fe)<br>$B \xrightarrow{k_2} C \xrightarrow{k_3} 2D$ |                          | Changeover Time (s)<br>$t_c$ | Percent Ferroxidase Reaction<br>% |
|----------|---|--------------------------|---------------------------|--------------------------|---|--------------------------|------------------------------|-----------------------------------|
|          | $k_1$ (s <sup>-1</sup> )  | $k_2$ (s <sup>-1</sup> ) | $k_2'$ (s <sup>-1</sup> ) | $k_3$ (s <sup>-1</sup> ) | $k_2$ (s <sup>-1</sup> )  | $k_3$ (s <sup>-1</sup> ) |                              |                                   |
| 48       | 81.3 ± 0.8  | 1.85 ± 0.03              | 0.484 ± 0.003             |                          |   |                          |                              | 100                               |
| 96       | 86.6 ± 6.3  | 1.92 ± 0.02              |                           | 0.694 ± 0.012            | 0.475 ± 0.041   | 0.168 ± 0.009            | 1.9 ± 0.4                    | 88 ± 10                           |
| 200      | 81.0 ± 2.7  | 2.16 ± 0.02              |                           | 0.614 ± 0.009            | 0.573 ± 0.050   | 0.148 ± 0.002            | 5.7 ± 0.9                    | 84 ± 8                            |
| 500      | 81.0 ± 4.6  | 1.83 ± 0.08              |                           | 0.61 ± 0.09              | 0.617 ± 0.012   | 0.042 ± 0.004            | 9.9 ± 0.3                    | 57 ± 5                            |
| 800      | 107 ± 5   | 2.65 ± 0.03              |                           | 0.821 ± 0.007            | 1.06 ± 0.02   | 0.081 ± 0.025            | 8.0 ± 0.3                    | 32 ± 4                            |

action, and Mössbauer spectroscopy demonstrated complete oxidation of the Fe(II).) At the changeover time,  $t_c$  ( $t_c = 3.2$  s for the 500 Fe sample of Figure 8), a new kinetic process takes over that we assume corresponds to clearance of the ferroxidase site according to the following reaction sequence (Mechanism II):



The absorbance as a function of time for this phase of the reaction is given by  $Y(\lambda, t) = \epsilon_B(\lambda)[B(t)] + \epsilon_C(\lambda)[C(t)] + \epsilon_D(\lambda)[D(t)]$ . The derived integrated rate equations for the concentrations of individual species are as follows:

$$B(t) = B(t_c)e^{-k_2\tau} \quad (24)$$

$$C(t) = B(t_c)\frac{k_2}{k_3 - k_2}(e^{-k_2\tau} - e^{-k_3\tau}) + C(t_c)e^{-k_3\tau} \quad (25)$$

$$D(t) = 2B(t_c)\left(1 + \frac{k_2e^{-k_3\tau} - k_3e^{-k_2\tau}}{k_3 - k_2}\right) + 2C(t_c)(1 - e^{-k_3\tau}) \quad (26)$$

Here,  $\tau = t - t_c$ , and  $B(t_c)$  and  $C(t_c)$  correspond to the concentrations of B and C present at the end of the plateau in Mechanism I, that is, at  $t = t_c$ . Figure 8 shows the fitted curve and residual for Mechanism I in the time interval of 0–3.2 s and for Mechanism II at times >3.2 s. The combination of Mechanisms I and II satisfactorily reproduce the key features of the 650 nm kinetic trace of Figure 8.

With exception of the 500 and 800 Fe/protein samples, which exhibit clearly defined plateaus, the time  $t_c$  corresponding to the changeover between Mechanisms I and II is not immediately obvious in the experimental data for the samples containing less iron (cf. Figure 1). In these instances, the changeover time,  $t_c$ , was initially estimated from the time point where the simulation using Mechanism I began to deviate from the experimental data. Using this time as a starting point,  $t_c$  was adjusted to minimize the residuals between the calculated (using Mechanisms I and II equations) and experimental data in the time interval,  $t_c, \pm 0.5$  s. Table 1 summarizes the values of  $t_c$  and the rate constants for the various samples derived from curve fitting of the data in Figure 1. The simulated curves for the 48, 96, 200, 500, and 800 Fe samples are also shown in Figure 1 and are within the experimental noise of the kinetic traces and, therefore, are not easily seen in the figure. The model reproduces quite well the kinetic curves at all levels of iron loading of the protein beyond 48 Fe(II)/protein.

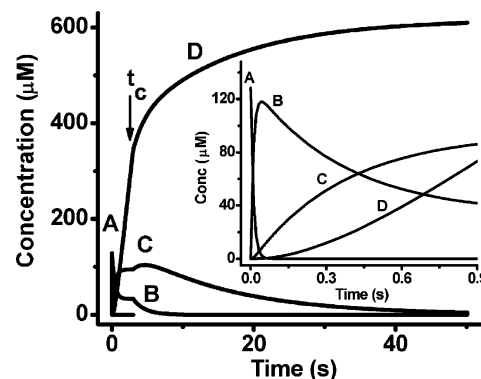


**Figure 9.** Simulation of the concentrations of A, B, C, and D species as a function of time using the rate constants in Figure 8. The inset shows the early portion of the reaction.

The percentage of iron that is processed by the ferroxidase pathway (eq 1) can be calculated from the total concentration of core,  $D_T$ , produced from the combination of Mechanisms I and II (eqs 19 and 26, respectively) and is given by  $\% = 100 \times D_T/Fe_T$ , where  $Fe_T$  is the total concentration of Fe added to the sample. The percentages are summarized in Table 1 for the different iron loadings of the protein preparation of Figure 1.

#### Species–Time Profiles for the >48 Fe/Protein Samples.

Figure 9 illustrates the concentration–time profiles of the various species calculated from the integrated rate equations for the 500 Fe sample of Figure 8. As expected, the concentration variable for all species in Figure 9 changes abruptly at the changeover time  $t_c = 3.2$  s between mechanisms. A small deviation is also observed in the residual of Figure 8 near  $t_c$  as the kinetics transition between the two mechanisms. As seen in the inset of Figure 9, both the peroxodiFe(III) species B and the  $\mu$ -oxo(hydroxo)diFe(III) species C achieve steady-state during Mechanism I. At the time  $t_c$ , the available Fe(II) has been consumed and the peroxo complex B is no longer formed; its concentration at the end of the plateau,  $B(t_c)$ , rapidly decays with a half-life of  $\sim 0.3$  s, causing a small rise in the concentration of C (Figure 9), a consequence of the smaller value of  $k_3$  in Mechanism II compared to that of Mechanism I. According to the model, C then decays slowly with a half-life of  $\sim 13$  s to form additional core D, and in the process, the ferroxidase site becomes cleared of its iron.

#### Discussion

Stopped-flow spectrophotometry has been employed in a number of qualitative and semiquantitative studies directed at elucidating the general reaction pattern and species formed in the very early stages of iron deposition in ferritin.<sup>14,18,23–27</sup> In the present work, a new analysis of the kinetics for the 48 Fe

sample reveals that the decay of the  $\mu$ -peroxo intermediate is not a simple exponential, as previously thought. The data strongly suggest that a second absorbing species ( $\lambda_{\max} = 655$  nm,  $\epsilon_B(655 \text{ nm}) = 570 \text{ cm}^{-1} \text{ M}^{-1}/\text{dimer}$ ) forms following the decay of the  $\mu$ -peroxodiFe(III) complex ( $\lambda_{\max} = 665$  nm,  $\epsilon_{B'}(665 \text{ nm}) = 840 \text{ cm}^{-1} \text{ M}^{-1}/\text{dimer}$ ). We tentatively ascribe this species, B', to a hydroperoxo complex with only one iron of the dinuclear center coordinated to the hydroperoxo group (Scheme 1). One expects that a hydroperoxo complex would exhibit a visible absorption spectrum similar to that of the peroxo complex as was found (Figure 5); however, its presence will require independent confirmation. In this connection, rapid freeze-quench Mössbauer spectroscopy of bullfrog M-ferritin has provided indirect evidence for a second (unidentified) intermediate following decay of the peroxo complex,<sup>35</sup> a finding in accord with the present stopped-flow data. A postulated reaction pathway leading to the putative hydroperoxo intermediate B' in the human protein is presented in Scheme 1 and involves breaking of the  $\mu$ -peroxo bond to one of the Fe(III) within the dinuclear structure, a first step toward the release of  $\text{H}_2\text{O}_2$  from the ferroxidase site complex into solution.

The peroxo complex B of human H-ferritin has a similar absorbance ( $\epsilon_B(650 \text{ nm}) \sim 850 \text{ cm}^{-1} \text{ M}^{-1}/\text{dimer}$ ) to that of bullfrog M-ferritin<sup>25</sup> ( $\epsilon_B(650 \text{ nm}) \sim 1000 \text{ cm}^{-1} \text{ M}^{-1}/\text{dimer}$ ) and is formed at a similar rate ( $k_1 \sim 80 \text{ s}^{-1}$ ) but decays somewhat more slowly ( $k_2 = 2.8$  versus  $4.2 \text{ s}^{-1}$ ). Unlike human H-ferritin where only a single oxo(hydroxo) dimer is evident in the first 10 s of the Fe(II) oxidation reaction,<sup>29</sup> the peroxo complex of bullfrog ferritin decays to multiple oxo(hydroxo) dimers and small clusters within the first second.<sup>35</sup> Multiple dimers and clusters do not appear in the human protein until minutes later.<sup>29,31</sup> Thus, although the two proteins have similar ferroxidase sites, the marked difference in species immediately produced upon decay of peroxo intermediate points to structural differences beyond their ferroxidase sites that influence the detailed kinetics and the species generated. Despite these differences, the human and bullfrog proteins efficiently form Fe(III) mineral cores through the oxidation of ferrous ion by dioxygen, a process that initially proceeds through a common peroxo (and probably hydroperoxo also) intermediate at the ferroxidase sites of both.

Stopped-flow spectrophotometry of the kinetics of the peroxodiFe(III) intermediate B at large fluxes of iron into the protein (up to 800 Fe/protein) demonstrates the involvement of the ferroxidase site in core formation at all levels of iron delivery to ferritin (Figure 1). Specifically, the marked changes in the kinetics profile of the intermediate with increasing amounts of added ferrous ion indicate that protein catalysis extends well beyond 48 Fe(II) added to the protein, the stoichiometric amount required to saturate the 24 ferroxidase centers with iron. Turnover of iron is evident from the extended time period in which the intermediate is observed at the higher levels of iron, ultimately developing a plateau in concentration followed by its decay. The analysis indicates that the percentage of ferroxidase center catalyzed iron oxidation (eq 1) progressively declines with increasing amounts of Fe(II) added (Table 1). That the ferroxidase reaction plays a role at higher iron loadings but to a declining degree is further supported by the observation that addition of Fe(II) to ferritin in increments of 50 Fe(II)/protein produces each time the transient blue color of the  $\mu$ -peroxodiFe-

(III) intermediate but with diminishing color intensity with each addition (result not shown). This decline in ferroxidase reaction is attributed to increasing importance of the detoxification and mineral surface reaction pathways (eqs 2 and 3) in forming the iron core.<sup>17</sup>

The two sequential mechanism model (Mechanism I + Mechanism II) nicely reproduces the principle features of the observed kinetics of all the >48 Fe samples (Figures 1 and 8). While there is some variation in kinetic properties between different protein preparations, the rate constants of Figures 1 and 8 with 500 Fe/protein are comparable ( $k_1 = 81.0 \text{ s}^{-1}$ ,  $k_2 = 1.83 \text{ s}^{-1}$ , and  $k_3 = 0.61 \text{ s}^{-1}$  versus  $k_1 = 89.5 \text{ s}^{-1}$ ,  $k_2 = 2.03 \text{ s}^{-1}$ , and  $k_3 = 0.72 \text{ s}^{-1}$  for Mechanism I, and  $k_2 = 0.617 \text{ s}^{-1}$  and  $k_3 = 0.042 \text{ s}^{-1}$  versus  $k_2 = 0.62 \text{ s}^{-1}$  and  $k_3 = 0.072 \text{ s}^{-1}$  for Mechanism II); they mostly differ in the extent of the plateau,  $t_c = 9.9$  versus 3.2 s. This difference in  $t_c$  values affects the calculated percentage of the core generated by the ferroxidase reaction for the two protein preparations, 57 versus 23% when 500 Fe(II) are added to the apoprotein. Hence, in the model, longer plateaus correspond to more iron being processed by the ferroxidase reaction of eq 1. The origin of the differences in  $t_c$  for different protein preparations is probably due to differences in the extent to which the rapid detoxification reaction of eq 2 competes with the ferroxidase reaction in each protein preparation (eq 1). The measured  $t_c$  value is reproducible from kinetic run to kinetic run for a given protein preparation.

A previous oximetry study of regeneration of ferroxidase activity in human H-chain ferritin indicated a half-life of  $\sim 5$  min for turnover of Fe(III) at the ferroxidase site when 48 Fe(II) are presented to the protein.<sup>16</sup> In Mössbauer studies, oxo(hydroxo)Fe(III) clusters formed from migration of Fe(III) from the ferroxidase site become evident in spectra only some 10 min into the reaction, consistent with slow Fe(III) turnover at the ferroxidase site.<sup>29,31</sup> In accord with these earlier results, the stopped-flow data for the 48 Fe sample indicate that, at 50 s (the last time point collected), only the  $\mu$ -oxo(hydroxo)diFe(III) ferroxidase site species C is present. There is no evidence for iron clusters that have UV spectra distinct from that of the dimer C.<sup>16</sup> Thus, the oximetry, Mössbauer, and the present stopped-flow kinetics measurements all demonstrate that iron turnover at the ferroxidase site is relatively slow when only 48 Fe(II) are presented to the apoprotein.

In contrast to the 48 Fe(II) samples, the analysis of the stopped-flow data of samples containing >48 Fe(II) shows rapid turnover of iron at the ferroxidase center. Turnover occurs with a half-life  $t_3 \sim 1$  s, corresponding to the  $k_3$  step of Mechanism I (eq 11), which is the rate-limiting step for formation of the mineral core D in Mechanism I (Table 1). The markedly faster rate of turnover of iron at the ferroxidase site in the >48 Fe/protein samples ( $\sim 300$  times faster than the 48 Fe/protein sample) indicates that the presence of excess Fe(II) facilitates this process in some way, ensuring that catalysis is continually maintained. This phenomenon possibly occurs through a yet to be identified effector site on the protein to which Fe(II) binds or simply through competition between Fe(II) and Fe(III) for binding at the ferroxidase site, where oxidized Fe(III) is replaced by fresh Fe(II) for the next cycle of catalysis.

Another interesting aspect to the kinetics data is the lower values of the rate constants  $k_2$  and  $k_3$  seen in Mechanism II compared to those of Mechanism I (Table 1). This slowed

bleaching during the Mechanism II phase of the reaction may be due to the  $\text{Fe}^{2+}$  being completely consumed at this final stage of iron deposition, whereby it no longer modulates the kinetics as discussed above. Also, it is important to note that ferritin is unlike a traditional enzyme in that the products of the reaction, namely,  $\text{Fe}^{3+}$  and its oxy(hydroxy) polymeric forms, are deposited inside the protein itself rather than being released into solution. The presence of such large amounts of  $\text{Fe}^{3+}$  in the mineral core as well as bound to the protein most likely has an effect on the rate constants obtained for different iron loadings of the protein, especially for the 500 and 800 Fe/protein samples compared to the others (Table 1). Despite these complications, the salient features of the stopped-flow data can be reproduced quite well using the kinetics models developed here.

In summary, the present work has provided new insights into the complex kinetics of ferritin iron biomineralization. The

unusual kinetic curves observed by stopped-flow spectrophotometry have been successfully simulated for all levels of iron loading of human H-chain ferritin, and a modulating effect of Fe(II) on turnover of Fe(III) at the ferroxidase site has been identified for the first time. The presence of an additional intermediate, postulated to be a hydroperoxo diFe(III) complex, is suggested by a detailed analysis of the kinetic data of 48 Fe/protein samples.

**Acknowledgment.** This work was supported by Grant R01 GM20194 from the National Institute of General Medical Sciences (N.D.C.), by the Italian Ministry of the University and Research (MURS) Cofin-2002 (P.A.), and by Fibr-2001 (P.A.). We thank Professor Georgia Papaefthymiou for the Mössbauer measurement on the 500 Fe/protein sample.

JA044355K